Bulletin of Earthquake Engineering (2026) 24:1905–1930
https://doi.org/10.1007/s10518-025-02360-1

ORIGINAL ARTICLE

Physics-based simulations of the foreshock and aftershock of the February 6, 2023 Turkiye earthquakes and ground motion validation

Bilal Ozaslan[1] · **Hiroaki Yamanaka**[2] · **Seiji Tsuno**[2] · **Nobuyuki Yamada**[3]

Received: 19 August 2025 / Accepted: 29 December 2025 / Published online: 8 January 2026

Abstract

This study presents the first three-dimensional (3D) physics-based ground motion simulations conducted for southern Turkiye, focusing on the foreshocks and aftershocks associated with the February 6, 2023 Turkiye earthquake sequence. The simulations were performed using a fourth-order staggered-grid finite-difference method developed for elastic media, incorporating a point-source double-couple representation to model rupture processes. Moderate-magnitude earthquakes were selected to enable the investigation of site-specific effects with reduced influence from the complex source characteristics typically associated with large events and from nonlinear behavior of near-surface soils. Accordingly, a regional-scale velocity model was constructed to capture both the source locations of these events and the dense strong-motion observation network covering Kahramanmaraş, Gaziantep, Türkoğlu, Nurdağı, and Pazarcık. The simulation results for both the Nurdağı (Gaziantep) Mw 4.5 aftershock on February 19, 2023 and the Pazarcık (Kahramanmaraş) Mw 4.5 foreshock on October 20, 2022 are analyzed by incorporating variations in the deep crustal velocity structure and low-velocity shallow sedimentary layers, with shear-wave velocities as low as 800 m/s. Simulated ground motions were compared with observed strong-motion records, and validation was carried out using a comprehensive set of intensity and frequency-based ground motion metrics. These included waveform similarity, Arias duration, energy duration, Arias intensity, energy integral, peak ground acceleration (PGA), peak ground velocity (PGV), peak ground displacement (PGD), response spectra, and Fourier amplitude spectra, following the quantitative fit scoring methodology based on synthetic-to-observed motion comparison metrics proposed by Anderson (Earthquake Engineering Research Institute, 2004). Strong-motion recordings were largely consistent with the simulations, with intensity-based fit scores predominantly in the 6–8 range and coherent response spectrum residuals in the 1–10 s period band, demonstrating the reliability of the results up to 1.0 Hz for long-period ground-motion assessment and for resolving contributions from both shallow and deep structural features. The study highlights the critical importance of capturing irregular wave propagation patterns shaped by regional stratigraphy and sedimentary basin configurations. Overall, the research provides essential methodological and modeling infrastructure to improve seismic hazard assessment and support resilient infrastructure planning.

Extended author information available on the last page of the article

Keywords Physic-based earthquake simulation · 3D seismic wave propagation · Staggered-grid finite-difference method · Kahramanmaraş earthquake 2023 · Ground motion validation

1 Introduction

On February 6, 2023, a devastating sequence of earthquakes struck southeastern Turkiye near the Syrian border, beginning with two major events with moment magnitudes of Mw 7.7 and Mw 7.6 as reported by the Disaster and Emergency Management Authority of Turkiye (AFAD), the principal governmental agency responsible for national seismic monitoring. The United States Geological Survey (USGS) reported these events as Mw 7.8 and Mw 7.5, respectively, while the Kandilli Observatory and Earthquake Research Institute (KOERI) provided magnitude estimates of Mw 7.8 for the 04:17 local time (UTC + 3) event and Mw 7.6 for the 13:24 event. These earthquakes occurred near the complex tectonic junction of the Anatolian, African, and Arabian plates, a region characterized by high seismic hazard due to active plate interactions (Duman et al. 2018). This unprecedented inland earthquake sequence, involving ruptures along segments of the East Anatolian Fault Zone (EAFZ) and the Dead Sea Fault Zone (DSFZ), was followed by an intense aftershock activity, significantly impacting a vast area. The most severe impacts were observed in densely populated cities such as Kahramanmaraş, Hatay, and Gaziantep, where basin structures and local site conditions are related to have contributed to the observed amplification of ground motions and the resulting damage. A thorough understanding of the physical parameters governing the spatial variability of ground motion, including seismic source characteristics, wave-propagation effects, and local site responses shaped by geological and geotechnical conditions, is crucial for accurately assessing structural damage in urban regions. Insights into these parameters are largely derived from systematic analyses of strong-motion datasets acquired in regions with dense seismic instrumentation and a history of major earthquake activity. Findings derived from these analyses directly facilitate the identification of ground motion amplification processes and their spatial correlation with documented damage patterns, consequently enhancing the development of advanced seismic design methodologies and resilience-oriented infrastructure planning (AFAD 2023).

However, the scale and complexity of the February 6, 2023 earthquake sequence presented significant challenges regarding the availability and quality of strong-motion recordings across the affected region. The scarcity of reliable near-fault ground motion recordings, particularly for the mainshocks, limits the ability to fully characterize the source rupture processes and near-field wave propagation effects. Even available waveform data from networks such as the Turkiye Earthquake Data Center System (TDVMS; https://tdvms.afad.gov.tr/) often required careful screening due to issues such as noise contamination, ambiguous signal onsets, early termination, delayed triggering, instrument malfunctions, or severe near-fault phenomena like clipping and large baseline offsets, leaving a limited number of usable records near the primary rupture zones (Buckreis et al. 2024a, b). These deficiencies underscore the difficulties in relying solely on observational data for a comprehensive ground motion analysis.

To bridge this data gap and enhance our understanding, physics-based numerical simulations of seismic wave propagation offer a powerful alternative. By solving the elastodynamic wave equation in heterogeneous media, these simulations can generate spatially complete, source-consistent ground motion time histories, providing critical insights for engineering applications and regional seismic hazard assessments (Graves and Pitarka 2015; Paolucci et al. 2021; McCallen et al. 2021). The fidelity of such simulations, however, is fundamentally dependent on the accuracy of the 3D subsurface velocity model representing the geological structure, including features like sedimentary basins known to significantly amplify seismic waves (Semblat et al. 2005; Makra and Chávez-García 2016).

Research into site effects and wave propagation in layered media has evolved significantly. Early studies utilized analytical or semi-analytical methods (Aki and Larner 1970), followed by the application of numerical techniques like finite differences and finite elements to explore wave phenomena in laterally varying structures (Smith 1975; Bard and Bouchon 1980; King and Tucker 1984; Kawase 1996). Numerous studies have focused on specific aspects, such as propagation through deep sedimentary layers (Yamanaka 1989), the influence of bedrock topography (Papageorgiou and Kim 1991), basin response (Zhang and Papageorgiou 1996), and amplification by shallow structure features (Graves 1998). While empirical adjustments to ground motion prediction equations can partially account for site effects (Somerville and Graves 2003), recent advancements in 3D numerical modeling, significantly boosted by the increasing power of high-performance computing enable more rigorous, physics-based site-specific and regional simulations (Khanbabazadeh et al. 2013; Chávez-García et al. 2018; Moczo et al. 2018; Zhu et al. 2018; Özaslan et al. 2020; Khanbabazadeh et al. 2022; Özaslan et al. 2022). These advancements now make regional 3D simulations up to frequencies relevant for engineering (~ 1 Hz or higher) computationally feasible.

Understanding and accurately predicting ground motion characteristics in irregular geological settings is paramount for seismic hazard assessment and risk mitigation strategies (Graves et al. 1998; Pitarka 1999). The development and refinement of regional models is crucial not only for minimizing epistemic uncertainties in physics-based simulations but also for advancing the scientific understanding of underlying fault mechanics. Despite this progress and various geophysical investigations in southern Turkiye, a validated, high-resolution 3D velocity model encompassing the extended Kahramanmaraş-Hatay region suitable for simulating ground motions up to engineering frequencies has been unavailable. Furthermore, although physics-based ground-motion simulations have been widely explored by international research groups, their implementation within Turkiye has been concentrated primarily in the Istanbul region, and the scarcity of integrated subsurface and site-specific data in most other areas continues to limit the broader adoption of validated 3D physics-based simulations for seismic hazard assessment. Responding to this critical need, particularly highlighted by the 2023 events, this study contributes by developing and rigorously evaluating the first regional 3D velocity model designed for the southeastern Turkiye region. Recognizing the complexities involved in accurately characterizing the seismic source of large earthquakes (e.g., Miyake et al. 2003; Yamada and Iwata 2005; Irikura and Miyake 2011; Taborda and Bielak 2011; Petersson and Sjogreen 2012; Zhang et al. 2019; Petrone et al. 2021; Pitarka et al. 2021), a necessary first step is the validation of the structural (velocity) model itself. Simulating a smaller-magnitude event, such as an aftershock, with a well-constrained, simpler source representation (like a point double-couple) allows for a focused evaluation of the path effects introduced by the 3D velocity structure, minimizing uncertainties related to inherently uncertain source processes.

To support improved seismic hazard characterization in the aftermath of the 2023 earthquake sequence, this study presents the development and performance evaluation of a 3D regional velocity model for southeastern Turkiye. The model incorporates both shallow sedimentary layers and deeper crustal structures that extend to the Moho, approximately 30 km in depth. Ground motion simulations were conducted for two moderate-magnitude earthquakes, specifically the Mw 4.5 aftershock near Nurdağı (Gaziantep) on February 19, 2023 and the Mw 4.5 foreshock near Pazarcık (Kahramanmaraş) on October 20, 2022. These simulations applied a point-source double-couple approximation and produced synthetic waveforms up to 1 Hz. The results were evaluated through detailed comparisons between synthetic seismograms and observations from the Turkish National Strong Motion Network. The assessment included waveform correlation, amplitude-based parameters such as Arias intensity and peak ground motions, frequency-domain measures involving spectral accelerations and Fourier amplitude spectra, and timing metrics represented by energy and significant duration. These comparative analyses yielded composite scores in accordance with established quantitative methodologies proposed by Anderson (2004). The results of the quantitative scoring assessment indicate that the simulated ground motions are reliable, and that the proposed velocity model provides a scientifically sound basis for future broadband simulations and scenario-based seismic hazard modeling. These outcomes enhance the regional understanding of ground motion characteristics and support the development of earthquake-resilient design strategies across southern Turkiye.

2 Physics-based 3D earthquake simulations

Performing 3D physics-based ground motion simulations, particularly at the higher frequencies relevant for engineering assessment, presents significant computational challenges. The computational effort required for simulating 3D wave propagation scales approximately with the fourth power of the maximum frequency resolved (f_{max}^4). Consequently, achieving a 1 Hz resolution demands a sufficiently fine computational mesh, especially in regions with low seismic velocities (V_{Smin}=800 m/s), leading to substantial computational cost and necessitating efficient numerical methods and High-Performance Computing (HPC) resources (Smerzini et al. 2023; McCallen et al. 2024).

This computational intensity underscores the importance of optimizing both the numerical framework and the characterization of earthquake sources. In parallel with these numerical developments, significant progress has been made in modeling seismic slip distributions on faults, typically through kinematic source models constrained by long-period seismic observations, such as strong-motion velocity or displacement records and teleseismic data. At such periods, ground motion behavior tends to be predominantly deterministic, allowing relatively simplified representations of source and crustal structure to reproduce waveform characteristics with reasonable accuracy. In contrast, modeling high-frequency strong ground motion remains substantially more challenging. These motions exhibit considerable randomness due to their sensitivity to fine-scale heterogeneities and the material anisotropy of near-surface layers. As a result, they are predominantly stochastic in nature, and their detailed waveforms generally remain beyond the reach of accurate simulation. For this reason, simulations conducted up to 1 Hz, where epistemic uncertainties are relatively lower, provide more reliable and consistent results within the modeled frequency range (Somerville et al. 1999).

In this study, we employed the Finite Difference Method (FDM) using a staggered-grid velocity–stress formulation as implemented in the FD3D code, originally demonstrated by Graves (1996) to be numerically stable, accurate, and consistent through comparisons with frequency–wavenumber solutions, and further developed and used in current simulation research by Yamada and Iwata (2005) at the Tokyo Institute of Technology. This explicit scheme solves the elastodynamic wave equation through time stepping. Simulations were carried out within a three-dimensional computational domain measuring 80 km × 80 km horizontally and extending to a depth of 30 km. To suppress artificial wave reflections at the model boundaries, absorbing boundary conditions were applied along the lateral sides and the bottom of the domain, while a free-surface condition was assigned at the top, ensuring physically realistic outward propagation of seismic waves. The model space was discretized using a uniform grid with a spatial resolution of $\Delta \mathrm{x} = \Delta \mathrm{y} = \Delta \mathrm{z} = 200\,\mathrm{m}$. This grid spacing ensures accurate simulation of wave propagation up to the target frequency of 1 Hz by maintaining approximately five grid points per minimum S-wave wavelength ($\lambda_{\mathrm{min}} = \mathrm{Vs}_{\mathrm{min}}/\mathrm{f}_{\mathrm{max}} \geq 4\Delta \mathrm{x}$) within the lowest velocity zones of the model. The total duration of each simulation was set to 100 s, and the time step was assigned according to the numerical stability condition ($\Delta \mathrm{t} \leq \frac{6\Delta \mathrm{x}}{7\sqrt{3}\,\mathrm{Vs}}$), which constrains the allowable time increment relative to the spatial grid spacing and the local shear-wave velocity. This criterion represents the stability limit for three-dimensional staggered-grid elastodynamic formulations (Graves 1996; Yamada and Iwata 2005).

2.1 Development of the 3D regional velocity model of Kahramanmaraş

As part of efforts to improve regional seismic modeling, 3D regional velocity model was developed for the source region of the February 6, 2023, Kahramanmaraş earthquake to accurately capture seismic wave propagation within a geologically and geotechnically heterogeneous environment. The model domain extends over an area measuring 80 km by 80 km, covering the Kahramanmaraş Basin as well as nearby urban centers including Gaziantep, Türkoğlu, Nurdağı, and Pazarcık. Shear-wave velocity ($\mathrm{V}_{\mathrm{s30}}$) values across the regional stations range from 280 to 1220 m/s, indicating variability in near-surface geological conditions, and these values were obtained from the AFAD Strong Motion Database and classified according to the Turkish Building Earthquake Code (TBEC-2018) site classification scheme. Stations such as KHMR (1220 m/s) and 2703 (756 m/s) represent rock or very stiff soil conditions. Intermediate Vs_{30} values, indicative of stiff soils or weathered rock, are recorded at stations 4618 (715 m/s), NAR (653 m/s), 2712 (599 m/s), 2709 (555 m/s), and 2708 (523 m/s). Lower Vs_{30} values, characteristic of soft sedimentary environments, are observed at stations 4622 (440 m/s), 4615 (485 m/s), 4624 (280 m/s), 4616 (390 m/s), and 4630 (347 m/s). Figure 1 provides a geographical overview of the February 6, 2023 earthquake sequence, the simulated events, the distribution of strong-motion stations, and the spatial extent of the Kahramanmaraş Basin.

A uniform grid spacing of 200 m was adopted in the finite-difference mesh, which permits the representation of near-surface structures with thicknesses on the order of 200–600 m. Within this resolution, the spatially averaged shear-wave velocities generally exceed

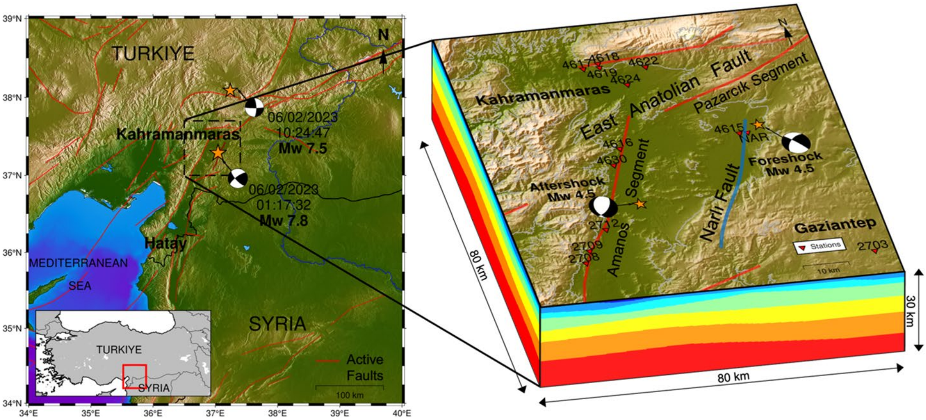

Fig. 1 The left map illustrates the epicentral locations of the two mainshocks of the February 6, 2023 earthquake sequence: the Mw 7.8 Pazarcık event (37.226°N, 37.014°E; 01:17:34 UTC) and the Mw 7.5 Elbistan event (38.011°N, 37.196°E; 10:24:48 UTC), both represented by stars. The right map displays the simulated foreshock and aftershock with Mw 4.5. The extent of the Kahramanmaraş Basin is indicated, and AFAD strong-motion recording stations employed in this study are marked with red triangles

800 m/s; consequently, the model incorporates velocities down to this threshold, whereas very low-velocity sediments (Vs < 400 m/s), which critically influence site-specific amplification, are not explicitly resolved. Such thin soft-sediment layers are inherently difficult to capture in regional-scale simulations and would require substantially finer grid spacing together with considerably greater computational resources. This limitation restricts to reproduce site-specific amplification effects in very shallow low-velocity layers, although it remains appropriate for assessing regional wavefield characteristics and supporting long-period seismic hazard evaluations. In this framework, shallow structures up to 200 m are integrated with deeper crustal units extending to 30 km, enabling a physically coherent representation of long-period wave propagation.

To establish the fundamental layered structure, seismic properties were derived from previously published crustal models and regional seismic investigations that employed geophysical methods. The deeper crustal structure, including distinct layer boundaries and velocity distributions, was constructed using results from surface-wave tomography, receiver-function analyses, and local earthquake tomography. These methods collectively provide constraints on large-scale velocity gradients, Moho depth, and crustal zones beneath southeastern Turkiye. Deep crustal and upper-mantle structures were primarily constrained using 3-D tomographic inversion of surface-wave data (Maggi and Priestley 2005), receiver-function (RF) analyses on broadband stations interpreted through genetic-algorithm–based inversion to obtain 1-D shear-wave profiles and Moho depths (Tezel et al. 2013), and local-earthquake tomography resolving heterogeneous crustal zones along the East Anatolian Fault Zone (Ozer et al. 2019). The shallow structure was constrained using microtremor array measurements at strong-motion stations in the region (Özmen et al. 2017). These datasets were merged by transforming the depth–velocity information from 1-D RF models, 2-D migrated RF sections, 2-D tomography slices, and 3-D regional crustal models into a uniform eight-layer parameterization, consistent with the requirements of the FD3D medium code structure. Depth interfaces obtained from these studies were gener-

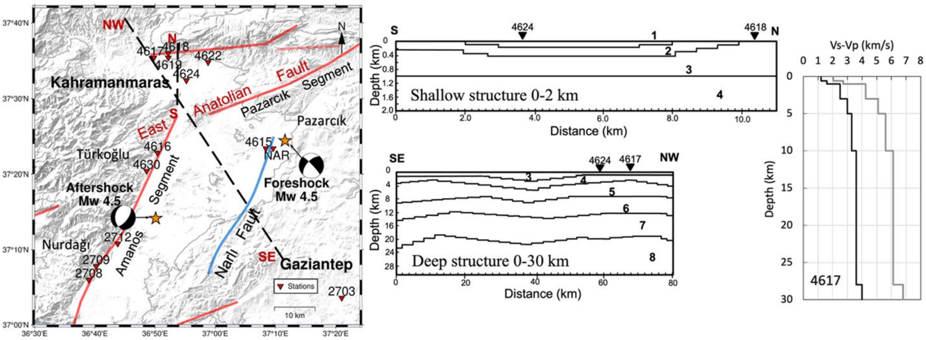

Fig. 2 The segments of the East Anatolian Fault and Narlı Fault are shown in red and blue on the map, while earthquake sources and strong-motion stations are indicated by stars and triangles, respectively. The central section illustrates two-dimensional geological profiles, showing the shallow subsurface layering in the upper image and deeper crustal structure down to the Moho depth in the lower image. These profiles are derived from the 3D regional velocity model covering the urban areas of Kahramanmaraş, Gaziantep, Nurdağı, Pazarcık, and Türkoğlu. On the right, Vs–Vp profiles are shown for station 4617, which is located near the city center of Kahramanmaraş

Table 1 Structural model parameters for the Kahramanmaraş region. Layer numbers correspond to the cross-sections presented in Fig. 2. Thicknesses vary spatially within the three-dimensional model

Layer no	H (km)	ρ (kg/m^3)	Vp (km/s)	Vs (km/s)	Q
1	0~0.2	1950	1.36	0.80	28
2	0.4~0.8	2150	2.04	1.20	49
3	0.6~2.4	2300	2.72	1.60	71
4	1.2~2.6	2500	3.65	2.15	106
5	3.2~5.4	2600	4.60	2.70	143
6	4.0~5.2	2680	5.10	3.00	165
7	6.0~9.0	2720	6.00	3.53	205
8	7~12.0	2900	6.80	3.99	241

Q values follow the formulation of Campbell (2009)

ated by applying pointwise linear interpolation between these depth–velocity control points across the entire finite-difference grid in both horizontal directions to generate continuous layer boundaries across the model domain. The interpolated horizons were mapped onto a uniform eight-layer structure, and each grid cell in the finite-difference mesh was assigned a material block code according to its depth. The resulting 3D model comprises eight primary layers that capture lateral and vertical variations in seismic properties. P-wave velocities (Vp) and densities were taken from these studies, and corresponding S-wave velocities (Vs) were computed assuming a regional Vp/Vs ratio of 1.7 (Zor et al. 2003; Medved et al. 2021). In addition, Fig. 2 provides a visual representation of the layer configuration together with the depth intervals of each stratigraphic unit. The detailed parameterization, including the spatial distribution and variability of Vp, Vs, density (ρ), and quality factor (Q), is also summarized in Table 1.

Seismic attenuation was modeled by assigning quality factors using an empirical relationship defined as $Q = 0.00382\, Vs^{1.333}$ (Campbell 2009), which reflects typical attenuation behavior observed in comparable geological materials. This formulation enables realistic simulation of wave energy loss during propagation, thereby ensuring that the model adequately captures the mechanical and anelastic behavior of both shallow sedimentary sequences and deeper crustal structures throughout the region.

2.2 Source characterization of the target earthquakes

Recent advancements in broadband ground motion simulation methods, such as those by Graves (1996), the Irikura and Miyake (2011) recipe, and Graves and Pitarka (2016), underscore the importance of realistic, physics-based kinematic rupture models for capturing faulting characteristics in large earthquakes. Although broadband simulations theoretically target frequencies from 0.1 Hz up to 10 Hz, practical implementations have only reached this upper limit within the last half-decade, primarily through state-of-the-art exascale computing efforts (McCallen et al. 2024). These approaches employ hybrid schemes that combine deterministic rupture asperity modeling with stochastic Green's functions to better resolve high-frequency content. The continued refinement of such methods, particularly through empirical relations of rupture parameters, has significantly enhanced their applicability to various earthquake scenarios, especially those involving intricate source characteristics. The selection of an appropriate earthquake source model for ground motion simulation is critical and is governed by the specific objectives of the study, the characteristics of the earthquake's focal mechanism, and the irregularity of the regional crustal velocity structure. The accuracy of the simulation depends on how well these factors are represented, as they significantly influence the propagation and amplitude of seismic waves (Zeng and Anderson 1996). Additionally, due to the inherent uncertainties of modeling nonlinear seismic response, which result from post-elastic deformation induced by high-energy excitations, and the challenges associated with defining finite fault models for such events, significant discrepancies often arise between recorded ground motions and simulation results. These factors present considerable obstacles to accurately incorporating nonlinear effects into the validation process of elastodynamic numerical methods. As further emphasized by Bizzarri (2014), achieving full physical realism is challenging, since it requires accounting for all geometrical features of the fault, spatial heterogeneities, stress drop distribution, and the dynamic forces acting along the rupture interface. However, applying these advanced models often requires comprehensive knowledge of the fault geometry and rupture process, which may not be readily available, particularly in the early stages of simulation-based studies in a given region.

In this context, the use of a point double-couple source not only ensures computational efficiency but also permits for the assumption of a constant slip rise time, a key parameter that defines the slip duration at a point on the fault surface and strongly affects the high-frequency content of radiated ground motion. Although direct observation of slip rise time is typically not feasible, it can be estimated through deterministic modeling that is calibrated against recorded ground motions. In rupture modeling practices, some approaches assume a constant slip rise time across the entire fault plane, while others incorporate spatial variability to reflect more realistic rupture dynamics. However, the ability to constrain spatial variations in slip rise time is significantly limited by the distribution, density, and azimuthal coverage of seismic recording stations. In this study, a simplified double-couple point-source representation was employed, for which a constant rise time is commonly assumed. Accordingly, a slip rise time of 1.0 s was adopted for both events based on empirical scaling relationships and parameters widely used in ground-motion simulations for moderate-magnitude earthquakes (Graves 1998; Graves and Pitarka 2016).

Furthermore, the selection of the Mw 4.5 aftershock was guided by the relative quality and availability of seismic recordings compared to other events in the 2023 Turkiye earthquake sequence. According to recent assessments (e.g., Buckreis et al. 2024a, b), many recordings from the mainshocks (Mw 7.8 and Mw 7.5) were affected by issues such as early termination (likely due to power failures), signal clipping, instrument saturation, and baseline correction problems. In contrast, the recordings from the selected aftershock exhibited fewer data quality issues, with greater spatial coverage, and provided more consistent broadband and accelerometer records. This enabled the assessment of ground motion simulations through the availability of high-quality observational data for model evaluation. In addition to the aftershock, the nearest recorded foreshock prior to the main rupture was also selected for comparison, enabling evaluation of the simulation framework under different rupture scenarios and ensuring temporal coverage of the sequence's seismic evolution.

For these reasons, initial modeling efforts in a newly studied regions commonly focus on small- to moderate-magnitude events using simplified source representations, such as point double-couple models. This approach provides an efficient and sufficiently accurate means of evaluating the simulation framework, while also isolating the effects of individual modeling components. In line with this strategy, moderate-magnitude earthquakes (Mw 4.5) were intentionally selected in this study to minimize the effects of rupture characteristics and nonlinear soil behavior. The source was modeled using a point double-couple representation derived from moment tensor solutions, providing a reliable means of capturing fault slip and stress release. Given the moderate magnitude and reduced source-related epistemic uncertainty of the selected events, a balance between physical realism and computational efficiency was achieved in the source characterization.

The moment tensor solutions for the selected Mw 4.5 earthquakes were obtained from the Turkish Disaster and Emergency Management Authority (AFAD) database: the Nurdağı (Gaziantep) earthquake on February 19, 2023, at 04:07:40 UTC + 3 local time (AFAD Event ID 16913) and the Pazarcık (Kahramanmaraş) earthquake on October 20, 2022 at 11:34:59, UTC + 3 (AFAD Event ID 14346). The foreshock (Mw 4.5) was located at a focal depth of 5.0 km with a source mechanism of strike = 180°, dip = 35°, and rake = −123°, whereas the aftershock (Mw 4.5) occurred at a depth of 8.3 km with a mechanism defined by strike = 316°, dip = 83°, and rake = −148°. The seismic moment values were computed following the empirical relationships provided by Irikura and Miyake (2011), based on the assigned moment magnitude of Mw 4.5 for both events. The rupture velocity adopted in this study falls within the commonly accepted range of 0.7Vs to 0.9Vs reported for crustal earthquakes (Mendoza and Hartzell 1989; Pitarka et al. 2020). Accordingly, a value of 0.85Vs was selected, consistent with standard kinematic rupture modeling practice (https://tadas.afad.gov.tr/event-detail/16913, and 14346).

3 Ground motion simulation results and quantitative validation analysis

3.1 Wave propogation on the regional model

An analysis of the simulated wavefield across the regional three-dimensional velocity model was conducted to examine the attenuation characteristics of seismic wave behavior, with particular attention to the temporal and spatial distribution of energy radiated from the source. The snapshots in Fig. 3 provide visual insight into the progression of seismic wavefronts generated by the Mw 4.5 aftershock, offering a qualitative understanding of wave behavior across the regional 3D structure. These time frames (5, 9, 12, 15, 18, and 21 s post-origin time) allow for a qualitative assessment of how the seismic energy radiates outward from the source and interacts with the layered subsurface conditions of southeastern Turkiye.

Early frames (5–9 s) highlight concentrated wave energy near the epicenter, with coherent circular fronts indicative of initial body-wave propagation. As time progresses (12–21 s), wavefronts expand radially, interacting with the structural heterogeneities of the basin. Observable wavefront distortion and amplitude variations become evident, particularly toward the north and east, indicating the influence of basin effects and lateral heterogeneities in the velocity model. The clear amplification and prolonged duration of waveforms as the fronts traverse the Kahramanmaraş basin and surrounding regions reflect both sedimentary

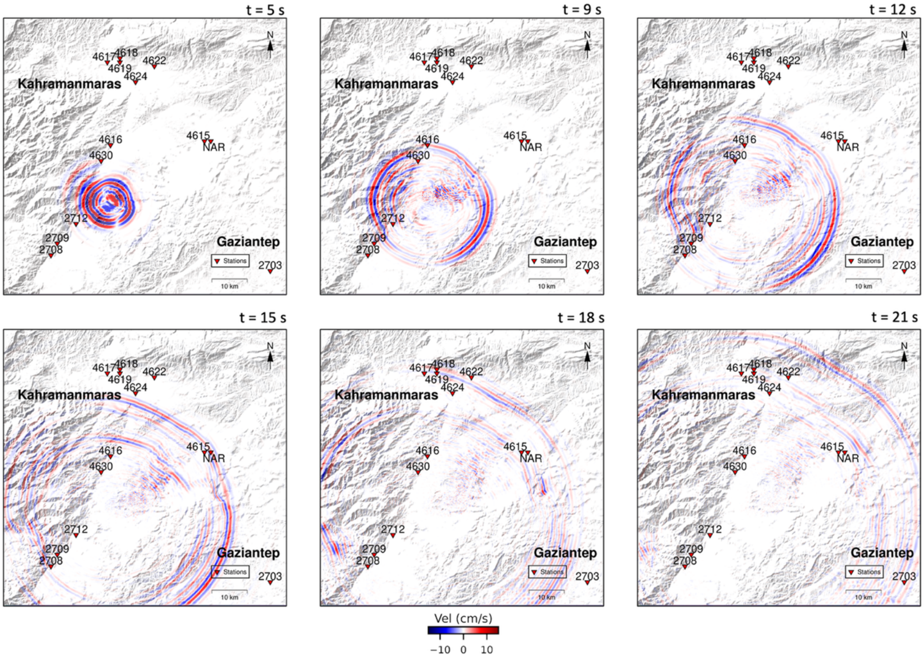

Fig. 3 Snapshots of horizontal (N–S) wave propagation generated by the Nurdağı (Gaziantep) Mw 4.5 aftershock on 19 February 2023 at 04:07:40 local time UTC + 3, displayed at 5 s, 9 s, 12 s, 15 s, 18 s, and 21 s from top to bottom. The unfiltered waveforms qualitatively depict the spatiotemporal distribution of seismic energy throughout the region

layering and crustal structure-induced scattering. The differential arrival times and interference patterns visible at stations such as 4616, 4624, and 2703 imply localized variations in wave speed and impedance contrasts.

Figure 4 presents the same sequence of six snapshots that depict the spatiotemporal evolution of the unfiltered horizontal (North–South) component of seismic wave propagation generated by the Mw 4.5 foreshock near Pazarcık. At approximately 3 s after rupture initiation, the seismic energy becomes visible at the surface near the epicenter, around stations NAR and 4615. Distinct circular wavefronts are evident and continue to expand radially with time. By 9 to 12 s, the wavefront reaches the central parts of the Kahramanmaraş basin, including stations 4616, 4617, 4618, and 4619. The temporal alignment of the wavefronts with known station locations provides a qualitative match with theoretical arrival times, supporting the validity of the propagation dynamics modeled. Between 15 and 21 s, the wavefield extends to broader regions, including southern stations such as 2703 (Gaziantep) and 2712. Compared to the Nurdağı aftershock shown in Fig. 3, the wave propagation in this event appears more distorted and spatially irregular, likely due to differences in the source mechanism, focal depth, or local geological conditions.

As the distance from the source increases, the wavefront begins to exhibit notable changes. First, there is a progressive reduction in amplitude, evident from the weakening waveform coloration, consistent with attenuation effects due to geometric spreading and intrinsic energy loss. Second, the shape of the wavefront becomes increasingly asymmetric, reflecting interactions with lateral variations in crustal structure, sublayer gradients, and potential basin-edge effect (Özaslan et al. 2022). Furthermore, complex wave interference becomes visible in the form of scattered energy and emerging codas behind the main wave-

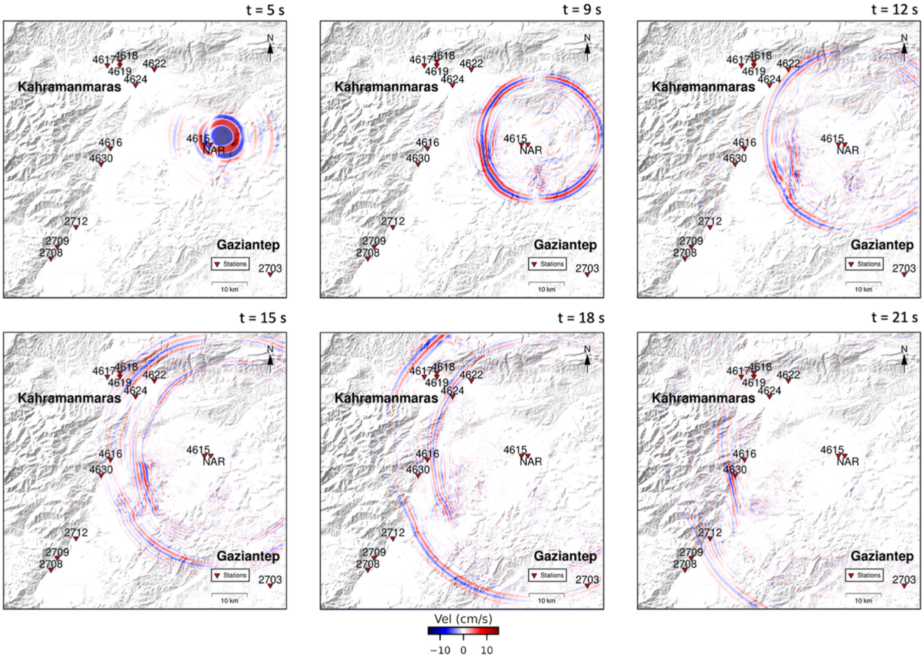

Fig. 4 Snapshots of horizontal (N–S) wave propagation generated by the Pazarcık (Kahramanmaraş) Mw 4.5 foreshock on 20 October 2022 at 11:34:59 local time UTC+3

front. These features suggest significant scattering and reflection within the heterogeneous crust, particularly at basin boundaries and stratigraphic transitions.

When considered together, Figs. 3 and 4 demonstrate the regional wave propagation characteristics for two moderate-magnitude events associated with the 2023 Kahramanmaraş earthquake sequence. The Nurdağı aftershock (Fig. 3) exhibits relatively symmetric and radially expanding wavefronts, with smoother energy distribution across the region. In contrast, the Pazarcık foreshock (Fig. 4) reveals more variable propagation patterns, including localized amplification and apparent directional focusing, especially in areas characterized by significant subsurface structure variability and sedimentary basins. These differences underscore the influence of both source properties and three-dimensional crustal structure on seismic wave behavior. Together, the figures validate the model's ability to capture realistic wavefield dynamics and highlight the critical role of regional heterogeneities in shaping ground motion characteristics across southeastern Turkiye.

Figures 5 and 6 provide a comprehensive evaluation of observed versus simulated ground velocity time histories, filtered within the 1–10 s period band. In Fig. 5, which corresponds to the Nurdağı Mw 4.5 aftershock, waveform comparisons are displayed for 13 stations across the region. Simulated traces are shown in red (N–S), blue (E–W), and green (vertical), while observed records are plotted in black. PGV values in cm/s are reported above each synthetic trace, allowing both visual and quantitative assessment of the waveform correspondence.

In Fig. 5, the synthetic time histories exhibit component-dependent discrepancies across the stations located within the Kahramanmaraş Basin. At stations 4618, 4619, 4622, and 4624, the simulated N–S components produce larger amplitudes than the observed motions. On the other hand, at stations situated closer to the source region near Türkoğlu and Narlı, including 4615, 4616, NAR, and 4630, the amplitudes of the vertical (U–D) components are overestimated. These discrepancies are likely influenced by near-source path effects, local subsurface heterogeneities, the simplified Q-model and vertical impedance contrasts, all of which can modify long-period energy partitioning and contribute to elevated vertical amplitudes in the simulations. Importantly, the timing of the primary arrivals and the characteristics of the later phases show notable similarities with the observed records.

In the southern part of the region, station 2712 exhibits consistent agreement across three components in terms of waveform characteristics and peak amplitude, whereas stations 2708, 2709, and 2703 (Gaziantep) show observed amplitudes that exceed the simulated values. Despite these amplitude differences, the timing of the arrivals remains broadly consistent across most stations, reflecting wave-propagation patterns that are coherent with the structure of the regional velocity model. Given the scale of the regional model, a certain amount of mismatch is expected due to necessary simplifications in shear-wave velocity distributions, attenuation properties and stratigraphic layering, and near-surface conditions beneath individual stations.

Figure 6 provides a station-by-station comparison of synthetic and observed ground velocity time histories for the Mw 4.5 foreshock that occurred near Pazarcık on October 20, 2022. Compared to the simulated aftershock results, the waveform matches in Fig. 6 shows greater variability. Several stations exhibit larger mismatches in amplitude, particularly in the vertical component. For instance, at station 4624, the simulated vertical trace significantly underestimates the observed amplitude. Similar underrepresentation in the vertical components is observed at stations 2708 and 2712.

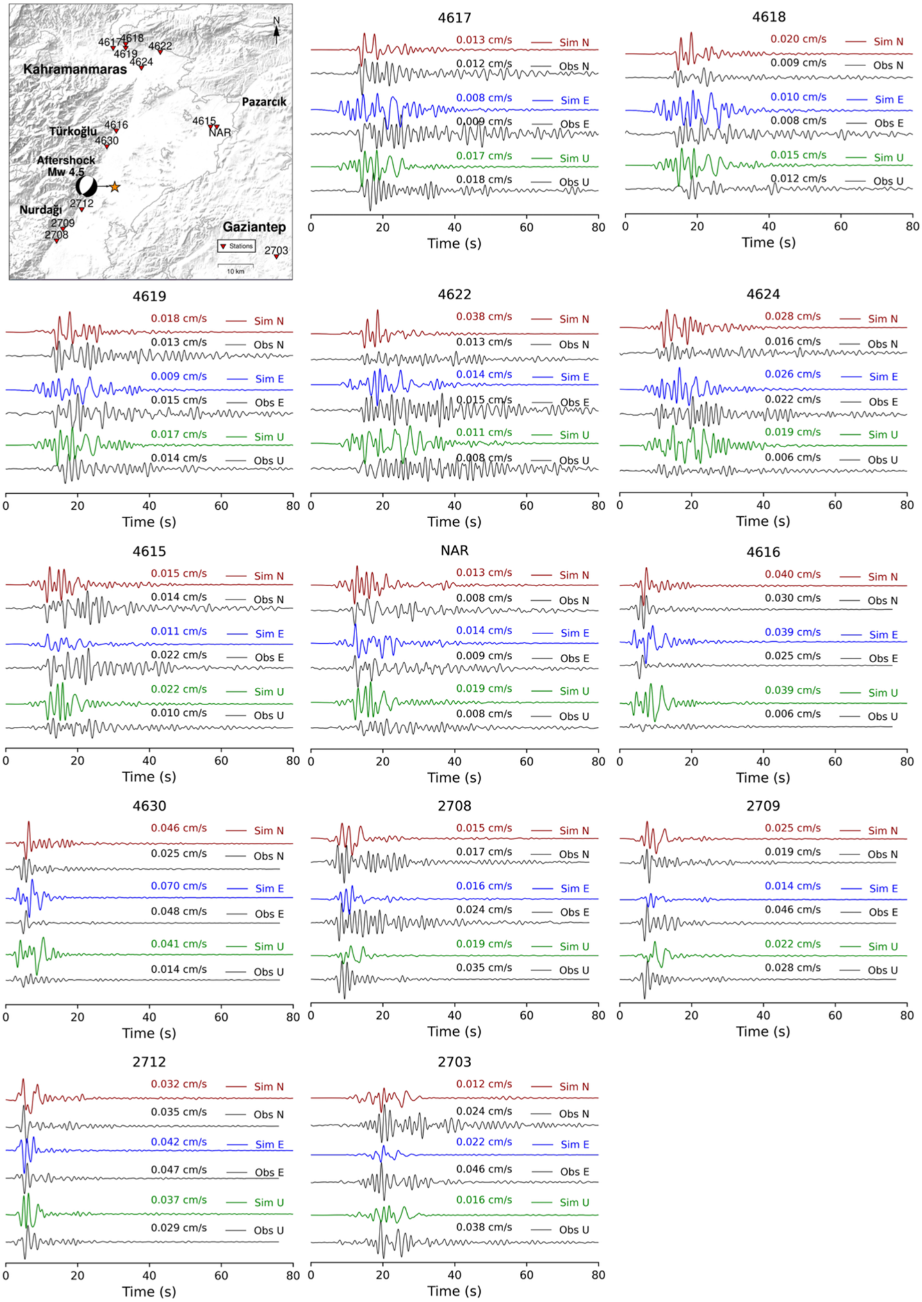

Fig. 5 Comparison of observed and simulated ground velocity time histories for the Nurdağı aftershock. Waveforms are band-pass filtered (1–10 s) and plotted with a uniform amplitude scale. Synthetic motions (red: N–S, blue: E–W, green: vertical) and observed motions (black) are shown. Peak velocities (cm/s) are indicated above each trace, and station locations are shown on the map

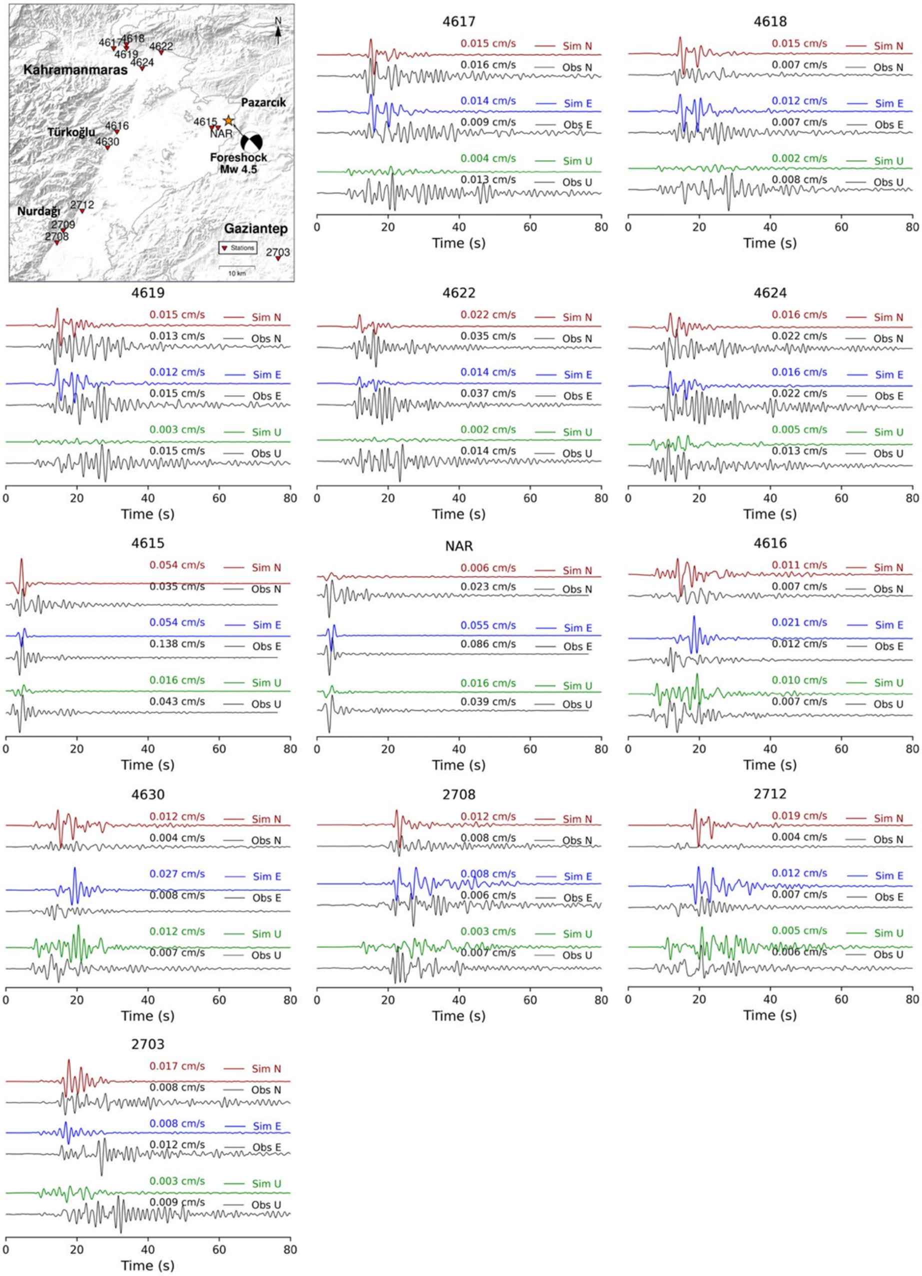

Fig. 6 Comparison of observed and simulated ground velocity time histories for the Pazarcık foreshock. Waveforms are band-pass filtered (1–10 s) and plotted with a uniform amplitude scale. Synthetic motions (red: N–S, blue: E–W, green: vertical) and observed motions (black) are shown. Peak velocities (cm/s) are indicated above each trace, and station locations are shown on the map

To further interpret the spatial variability in waveform agreement, a comparative analysis between the northwestern stations and the southeastern station 2703 was conducted. Analysis of the stations located northwest of the source (4617, 4618, 4619, 4622, and 4624) in comparison with the southeastern station 2703 indicates that the amplitude distribution observed in Fig. 6 is influenced by both epicentral distance and regional subsurface structure. Although stations 4617, 4618, and 2703 are situated at comparable epicentral distances of approximately 38 km, 37 km, and 40 km, respectively, the expected reduction in amplitude at station 2703 is evident in the observed records. For most of the northwestern stations, this distance–amplitude relationship is preserved; however, the observed three components at station 4618 and the E–W component at station 4617 deviate from the expected pattern. The simulation results reproduce this behavior only partially: the amplitude contrast between the northwestern stations and 2703 appears clearly in the E–W components, while the N–S components show this pattern only at station 4622. This component-dependent inconsistency suggests that long-period radiation characteristics are sensitive to subtle variations in the source geometry. Even modest changes in strike, rake, or dip can alter azimuthal energy distribution, which helps explain why the expected amplitude alignment—consistent with a NW–SE or NE–SW oriented fault plane—is distinct in the E–W components but less pronounced in the N–S directions. In addition, the structurally complex geological setting, particularly the deep and low-rigidity sedimentary layers ($Vs \approx 800$ m/s) underlying the Kahramanmaraş Basin and the Gaziantep region, introduces spatial heterogeneity that modifies long-period wave propagation and contributes to variations in peak ground velocities beyond those predicted solely by epicentral distance. These combined source- and structure-related effects account for the amplitude variability and component-dependent discrepancies observed across stations with similar epicentral distances in Fig. 6.

The comparative evaluations of Figs. 5 and 6, which present observed and simulated ground velocity time histories for the Nurdağı aftershock and the Pazarcık foreshock, qualitatively examine the performance of the regional velocity model in capturing long-period ground motion characteristics across southeastern Turkiye. In both the aftershock and foreshock simulations, the comparison between observed and synthetic ground motions reveals component-dependent similarities as well as notable discrepancies in their long-period characteristics. These differences reflect the combined influence of source specifications and the limitations inherent in representing shallow velocity structures within a regional-scale model. Overall, the comparative evaluation of the two events demonstrates that although several features of long-period wave propagation are approximated, finer- scale near-surface structural conditions remain more difficult to reproduce accurately.

As a result, achieving uniformly high agreement across all components and stations is generally attainable only in models constructed with very high spatial resolution and supported by extensive field investigations, both of which require substantial financial and computational resources. Such levels of detail are becoming increasingly feasible as high-performance computing technologies advance and as larger budgets are allocated to dense geophysical surveys and site-specific characterization efforts. For this reason, the primary objective in regional-scale modeling is to construct computationally feasible frameworks based on geological and geophysical assumptions that can reliably predict long-period ground motions with a quantitatively acceptable level of accuracy. In line with this objective, the following section employs ground-motion similarity proxies to quantitatively evaluate the performance of the regional velocity model and to assess its ability to reproduce long-period seismic wavefields. To further assess the applicability of the simulated ground motions in engineering analyses, particularly in seismic demand estimation, performance-based structural design, and seismic hazard studies, a comprehensive quantitative evaluation is required. As presented in the following section, this evaluation quantifies key parameters such as energy content, peak amplitudes, and signal durations in both the frequency and time domains.

3.2 Quantitative proxies for evaluating synthetic ground motions

In recent decades, the validation of synthetic strong ground motions has emerged as a fundamental objective in simulation-based earthquake research. While large-scale numerical models have enabled increasingly realistic representations of seismic wave propagation, they often exclude shallow subsurface stratigraphy due to the substantial computational cost associated with detailed 3D simulations. This limitation can compromise the predictive reliability of ground motion outputs. Importantly, the practical applicability of synthetic records in engineering analyses depends on the outcomes of comprehensive and multi-parameter quantitative evaluations. Effective validation, therefore, requires systematic, event-specific comparisons across a representative set of strong-motion stations. However, interpreting these comparisons is frequently complicated by the combined effects of source-related complexity, lateral crustal heterogeneities, and nonlinear site response. These interacting factors can obscure the distinct contribution of the velocity model to the simulated wavefield, highlighting the necessity for targeted evaluation approaches that isolate and quantify its role within the broader modeling framework.

The proposed goodness-of-fit evaluation builds upon the methodology introduced by Anderson (2004) and subsequently implemented by Tsuno et al. (2023), enabling quantitative assessment of both physical and signal-based characteristics of seismic ground motions. This approach is particularly well-suited for assessing the fidelity of synthetic seismograms relative to observed data. The evaluation employs a suite of intensity and frequency-based ground motion metrics, including Arias duration, energy duration, Arias intensity, energy integral, peak ground acceleration (PGA), peak ground velocity (PGV), peak ground displacement (PGD), response spectra (with 5% damping), Fourier amplitude spectra, and averaged scores, labeled as C1 ~ C9 and C_{AVE}. An average fit score is derived from nine individual quality measures. These metrics are defined by Eq. (1) through (10) and their corresponding mathematical definitions are summarized as follows.

$$SDa = 10\left|1 - max\left(F^{IA}(t)\right)\right|, \ where \ F^{IA}(t) = \left|N_1^{IA}(t) - N_2^{IA}(t)\right|, \ \ N^{IA}(t) = \frac{I_A(t)}{IA} \tag{1}$$

$$SDe = 10\left|1 - max\left(F^{E}(t)\right)\right|, \qquad where \ F^{E}(t) = \left|N_1^{E}(t) - N_2^{E}(t)\right|, \qquad N^{IE}(t) = \frac{I_E(t)}{IE} \tag{2}$$

In both metrics (C1 and C2), $I_A(t)$ and $I_E(t)$ denote the cumulative Arias intensity and cumulative energy, respectively, up to time t, while IA and IE are the total Arias intensity and energy over the entire duration of the record. The normalized cumulative functions $N^{IA}(t)$ and $N^{IE}(t)$ describe the accumulation of energy or intensity as a function of time. The differences $F^{IA}(t)$ and $F^{E}(t)$ represent the absolute deviations between the normalized observed and simulated records. The maximum of these differences across time quantifies the greatest mismatch in temporal evolution. Subtracting this maximum value from 1 and scaling by 10 transforms it into a similarity score ranging from 0 (poor match) to 10 (perfect match). These duration-based metrics effectively capture how well the simulations reproduce the temporal energy accumulation of real ground motions, which is critical for characterizing shaking duration and cumulative damage potential.

$$SIa = S\left(IA_1,\, IA_2\right),\ where\ IA_i = I_{Ai}\left(T_d\right),\ I_{Ai}\left(t\right) = \frac{\pi}{2g}\int_{0}^{t} a_i^2\left(t\right)dt \tag{3}$$

$$SIv = S\left(IE_1,\, IE_2\right),\ where\ IE_i = I_{Ei}\left(T_d\right),\ I_{Ei}\left(t\right) = \int_{0}^{t} v_i^2\left(t\right)dt \tag{4}$$

Where $a_{i(t)}$, $v_{i(t)}$, $d_{i(t)}$: acceleration, velocity, and displacement time histories for record i, defined over $0 \leq t \leq T_d$, where T_d is the total duration of the motions. $I_{Ai}\left(t\right)$ and $I_{Ei}\left(t\right)$ are Arias intensity (C3) and energy integral (C4), respectively.

$$Spga = S\left(A_1,\, A_2\right), \tag{5}$$

$$Spgv = S\left(V_1,\, V_2\right), \tag{6}$$

$$Spgd = S\left(D_1,\, D_2\right) \tag{7}$$

Where $A_i = max\left|a_i\left(t\right)\right|$, $V_i = max\left|v_i\left(t\right)\right|$, and $D_i = max\left|d_i\left(t\right)\right|$, represent the peak ground acceleration, peak ground velocity, and peak ground displacement, respectively, of the i_{th} component, derived from either recorded or simulated time histories, and used in metrics C5, C6, and C7.

$$Ssa = mean\left[S\left(SA_1\left(f_j\right),\, SA_2\left(f_j\right)\right)\right], \tag{8}$$

$$Sfs = mean\left[S\left(FS_1\left(f_j\right),\, FS_2\left(f_j\right)\right)\right] \tag{9}$$

Where $SA_i\left(f_j\right)$, $FS\left(f_j\right)$: spectral acceleration and Fourier amplitude spectrum of the i^{th} accelerogram at frequency f_j, used in metrics C8 and C9.

Among the employed proxies, a general similarity function is used to quantitatively assess the agreement between observed and simulated values across various ground motion parameters. This function is defined as follow:

$$S\left(p_1, p_2\right) = 10\,exp\left(-\left(\frac{p_1 - p_2}{min(p_1,\, p_2)}\right)^2\right) \tag{10}$$

Where p_1 and p_2 represent the observed and simulated values of a given parameter. The function returns a score ranging from 0 to 10, with higher values indicating stronger agreement.

All comparisons are based on records that have been band-pass filtered between 0.1 Hz and 1 Hz to ensure consistency in frequency content and to minimize low-frequency drift and high-frequency noise. Each metric is scored on a scale from 0 to 10, and the overall fit score is computed as the average of the individual metric scores. An overall score below 4 indicates poor agreement, values between 4 and 6 denote fair agreement, scores between 6 and 8 represent good agreement, and scores above 8 reflect excellent fit.

Figures 7 and 8 present the distribution of similarity scores for the Nurdağı (Gaziantep) Mw 4.5 aftershock and the Pazarcık (Kahramanmaraş) Mw 4.5 foreshock simulations, respectively. For each strong-motion station, nine individual goodness-of-fit metrics (C1–C9) were computed across three motion components: East–West (blue squares), North–South (red triangles), and vertical (green circles). This component- specific representation facilitates the assessment of directional variability in the agreement between simulated and observed waveforms. The average of the nine similarity scores is illustrated by a bar graph placed at the beginning of each station's row, providing a concise summary of the overall model performance at each location. This comparative analysis enables a systematic evaluation of the model's ability to reproduce observed ground motions across different stations and motion directions.

Horizontal components (red and blue traces) tend to yield higher and more consistent scores than the vertical component (green), particularly at stations 4616, NAR, 2708, and 2709. This indicates better waveform agreement in horizontally polarized ground motions, which may be attributed to the source radiation pattern or basin-related amplification effects. Stations located closer to the epicenter, such as 2712 and 4630, exhibit a wider variation

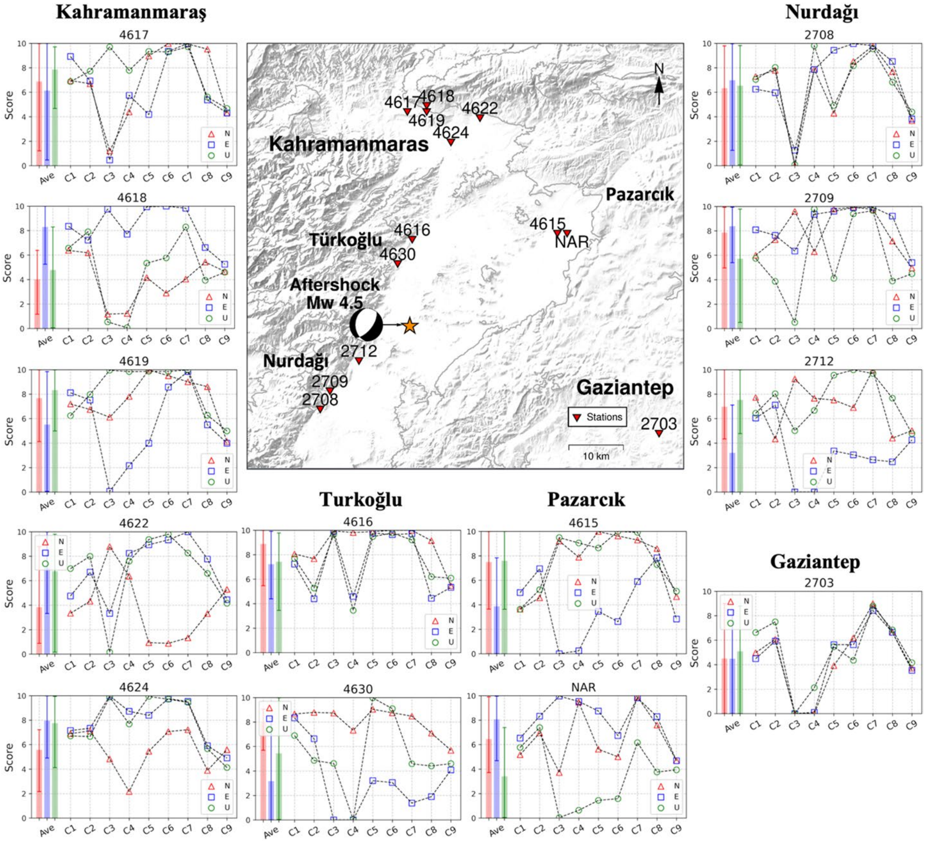

Fig. 7 Similarity score distribution for the Mw 4.5 Nurdağı (Gaziantep) aftershock simulation. Scores are shown for three components: East–West (blue squares), North–South (red triangles), and vertical (green circles). The bar graphs represent the average of the nine individual fit scores

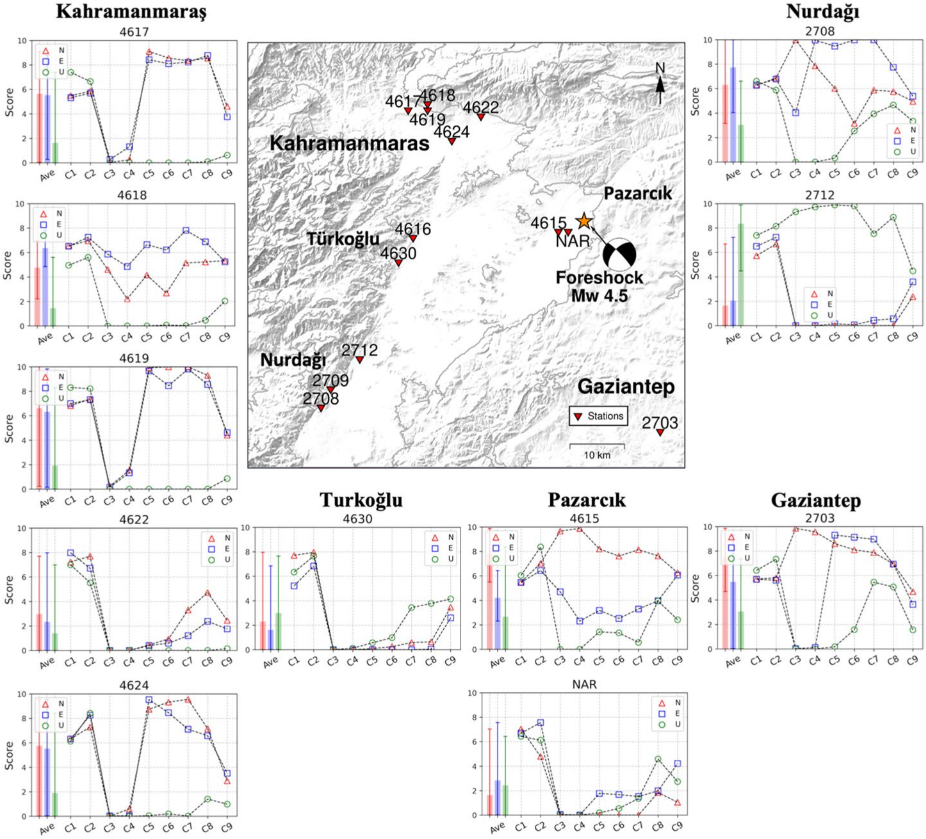

Fig. 8 Distribution of similarity scores from the Mw 4.5 Pazarcık foreshock simulation. The conventions for symbols, colors, and bar graphs are identical to those in Fig. 7. Some stations were excluded because clipped or incomplete observational records prevented stable computation of the quantitative proxies

in scores across components and metrics, potentially due to more irregular wave interference and near-field effects. In contrast, stations located farther from the epicenter, such as station 2703 in Gaziantep, exhibit average scores across the three components that are relatively close to one another. However, the reduced seismic energy reaching these distant sites, particularly affecting cumulative energy-related metrics such as C3 and C4, results in overall similarity scores remaining within the range of 4 to 5. Additionally, in Fig. 7, the low similarity scores across proxies C3–C7 in the N–S components at stations 4618 and 4622 are likely governed by basin-edge effects. Both stations are located near the northern basin edge of the Kahramanmaraş Basin, where the superposition of incident SV and P waves with waves reflected and refracted at the basin inclined boundary can produce localized amplification. This mechanism is consistent with previous numerical and observational studies on basin-edge amplification (Ozaslan 2022; Khanbabazadeh et al. 2022). Overall, the majority of comparisons for the aftershock demonstrate good to moderate agreement between observed and simulated ground motions, with average similarity scores across all three components generally falling within the 6 to 9 range.

Compared to the Nurdağı aftershock (Fig. 7), the Pazarcık foreshock (Fig. 8) demonstrates greater spatial variability in similarity scores across the region, indicating a wider range of waveform agreement. Several stations, including 4622, NAR, and 4630, exhibit substantial misfits across all three components, frequently resulting in considerably lower scores. Horizontal components (N and E) generally retain moderate to high similarity scores at many stations, underscoring their relative robustness in simulating seismic energy propagation. With the exception of station 2712, nearly all sites reveal marked inter-component variation, particularly characterized by reduced vertical component scores (green) in metrics C3 to C6. This pattern may be attributed to limitations in vertical site response modeling arising from localized heterogeneities in the near-surface velocity structure.

In Fig. 8, stations in the Kahramanmaraş area record high scores in the horizontal components, indicating that wave propagation is accurately represented in this region. Similarly, station 2708 (Nurdağı) shows strong agreement in the horizontal components, whereas station 2712 stands out with notably lower scores. This reduction may be attributed to its transitional geological setting, located between soft sedimentary layers and more rigid bedrock formations, which may produce increased variability in wave transmission. In comparison with the aftershock case, the lower similarity scores observed in the foreshock simulation, particularly for metrics C2 to C6, may originate from the specific parameters used in the foreshock source model, including the adopted moment tensor solution and energy distribution.

Stations such as 2712, 4622, 4630, and NAR exhibit notably low similarity scores during the Pazarcık foreshock simulation. Based on the AFAD strong-motion station database, these sites possess relatively low V_{S30} values, typically between 347 m/s and 653 m/s, consistent with soft to intermediate sedimentary conditions. Their close proximity to the epicenter, ranging from approximately 10 km to 33 km, places them within the near-field region, where complex wave interference, rupture directivity, and vertical ground-motion amplification commonly exert strong influence on long-period waveform characteristics. While the velocity model used in this study incorporates shallow layers down to 800 m/s, it does not resolve the full spectrum of the slower near-surface velocities that are essential for representing site-specific amplification in soft sedimentary environments. This limitation was initially considered the primary explanation for the poor fit observed at these stations. However, Fig. 7 (Nurdağı aftershock) shows that the model achieves reasonable performance at the same locations despite these structural simplifications, indicating that the reduced similarity in Fig. 8 is more likely attributed to the source characterization of the foreshock. In addition, several stations were excluded from Fig. 8 because their observational records contained clipping or incomplete time windows, preventing stable computation of the quantitative proxies.

This contrast may be attributed to differences in the source characteristics between the foreshock and aftershock events. In addition, localized velocity heterogeneities and nonlinear site effects, which are not fully captured in the current model, may have interacted more strongly with the foreshock source. Consequently, the discrepancies observed in the foreshock case cannot be solely attributed to the exclusion of sub-800 m/s layers; they are more likely the result of a combination of source complexity, wavefield interference, and local site conditions.

In general, the validation results of this study indicate that the horizontal ground motion components tend to be better reproduced, as evidenced by the prevalence of similarity

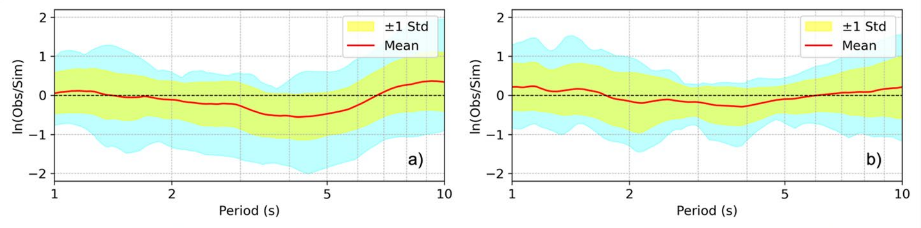

Fig. 9 Spectral acceleration residuals of RotD50 for horizontal components comparing observed and simulated ground motions in two events, graph (**a**) shows results for the Nurdağı aftershock and (**b**) for the Pazarcık foreshock. Logarithmic residuals (ln[Obs/Sim]) are plotted across a period range of 1 to 10 s. Solid lines represent the average residuals across all stations, while shaded regions indicate ± 1 standard deviation and the full residual range

scores exceeding 6. This finding reflects a reasonable level of agreement between observed and simulated records within the current modeling framework. Further improvements may be realized by increasing spatial resolution and incorporating a broader range of earthquake events with varying source characteristics.

4 Discussion

This study provides a significant and novel contribution to regional seismic modeling by presenting the first application of physics-based ground motion simulations specific to southeastern Turkiye, focusing on the development and validation of a 3D regional velocity model constructed in response to the destructive 2023 Kahramanmaraş earthquake sequence. The model incorporates key geological features of the region, including crustal structures extending to the Moho (~ 30 km), which strongly influence seismic wave propagation. The finite-difference modeling framework utilized in this study, selected for its proven numerical stability and computational efficiency, facilitated the simulation of moderate-magnitude fore- and aftershocks up to 1 Hz (Pitarka et al. 2004). Validation was conducted through detailed comparisons between synthetic and recorded ground motions using a suite of quantitative metrics. These comparisons consistently demonstrated moderate to good agreement at most stations.

To further evaluate the results, the RotD50 response spectrum is analyzed, which quantifies the geometric mean spectral acceleration at the orientation representing typical structural response, averaged over all horizontal directions. This rotationally invariant metric is widely adopted in seismic engineering due to its robustness and direct relevance to structural performance. Figure 9 presents a residual analysis between observed and simulated RotD50 spectral accelerations across a broad period range (1–10 s), expressed as the logarithmic ratio ln(Obs/Sim). The mean residual curve demonstrates a near-zero bias, indicating strong agreement between synthetic and recorded motions, while the ± 1 standard deviation bands and the full min–max envelope confirm that interstation variability remains within acceptable bounds. Notably, even at periods up to 2 s ($T < 2$ s), where simulation challenges such as limited resolution and attenuation-related uncertainties typically become more significant, the residual spread remains limited, underscoring the model's capability to capture key frequency-dependent characteristics of wave propagation. These results reinforce the conclusions drawn from waveform and similarity score analyses, affirming the reliability of the 3D regional velocity model in reproducing the spectral content of long-period ground motions.

While the current simulation bandwidth is limited to 1 Hz due to computational constraints, the presented framework establishes a scalable platform for future developments. Enhancing simulation frequency content to 5 Hz and beyond is crucial for capturing the higher-frequency demands of mid- to low-rise structures and critical infrastructure. Achieving this will require implementation on high-performance computing (HPC) systems with GPU-based acceleration and optimized parallel processing. In addition, extending the model to incorporate nonlinear site response and detailed velocity structures in urban basins will improve its ability to predict amplification effects and spatial variability in ground shaking.

As physics-based simulations become increasingly integrated into seismic hazard analysis, explicitly addressing modeling uncertainties has become essential. Significant progress has been driven by large-scale computational frameworks such as the Southern California Earthquake Center's *CyberShake* platform (Graves et al. 2010) and the exascale *EQSIM* workflow (McCallen et al. 2024), which collectively advance fault-to-structure simulation capabilities through the use of SW4, a fourth-order summation-by-parts finite-difference code for 3D seismic wavefield modeling (Petersson and Sjögreen 2015). Together, these developments illustrate how modern high-performance computing platforms enable fully integrated, multi-scale, physics-based ground-motion simulations.

Research on validating physics-based ground-motion simulations against past earthquakes has traditionally focused on their ability to reproduce intensity measures in an average sense. However, comparing simulations solely with empirical ground-motion models is insufficient, because the apparent variability in empirical predictions is strongly influenced by the functional assumptions of those models. Therefore, uncertainties in simulation outputs must be evaluated directly against observational strong-motion data to ensure that the physical variability of the earthquake system is adequately represented (Bradley 2019).

Growing confidence in average predictive performance has motivated recent advances addressing modeling uncertainties in physics-based simulations. Studies examining variability in kinematic rupture parameters (e.g., Graves and Pitarka 2016) demonstrate that uncertainties in magnitude, slip distribution, and stress drop can generate substantial variations in both long- and short-period motions. As shown in Fig. 9, the relatively low standard deviations reported at long periods highlight a key advantage of physics-based ground-motion modeling, the ability to capture large-scale source and crustal features that govern long-period wave behavior. Continued improvement in source, path, and site characterization is expected to extend this improved performance toward shorter vibration periods.

Future research will also benefit from the integration of multiscale modeling strategies, enabling the coupling of regional wave propagation with localized soil–structure interaction (SSI) models. This is particularly important for simulating infrastructure response under reliable ground motions that incorporate basin effects, rupture directivity, and stratigraphic influences. Such integration will also facilitate scenario-based simulations that account for source characteristics, thereby enhancing the robustness of seismic hazard assessments.

In summary, this study demonstrates the feasibility and value of physics-based simulations for regional seismic hazard assessment in Turkiye. The proposed methodological framework, supported by rigorous validation and comprehensive spectral analysis, provides a robust foundation for future high-resolution, physics-informed modeling. These advancements are expected to contribute to the development of more reliable ground motion prediction methodologies and the design of earthquake-resilient infrastructure in tectonically active regions.

5 Conclusion

Although the current study provides a robust framework for long-period ground motion simulation, critical limitations persist that require continued exploration. The deterministic simulations are constrained to frequencies up to 1.0 Hz, suitable for evaluating the behavior of long-period structures and base-isolated systems but insufficient for accurately representing the seismic demand on mid- and low-rise buildings, which are sensitive to higher-frequency content. While source-to-structure predictions within this frequency range offer valuable insight, extending simulations to capture higher frequencies remains challenging due to the limited resolution of geological and source parameterization. To bridge this gap, stochastic simulation methods are often employed beyond 1 Hz to account for epistemic uncertainties and small-scale heterogeneities not explicitly resolved in the deterministic model. Advancing simulation capabilities toward 5 Hz and beyond will require the integration of nonlinear site response analysis, improved near-surface geotechnical data, and high-performance computational strategies. Moreover, linking regional wave propagation models with site-specific soil and structural response models is essential for capturing localized amplification effects and for supporting performance-based earthquake engineering applications. Moreover, optimizing the simulation framework for next-generation high-performance computing platforms will enable the efficient execution of large-scale scenario modeling, including multiple realizations of accurately modeled fault ruptures. These advancements will significantly enhance the realism and applicability of ground motion simulations, thereby contributing not only to the refinement of regional seismic hazard models and the development of earthquake-resilient infrastructure across Turkiye, but also offering valuable methodologies applicable to other seismically active regions worldwide.

Acknowledgements This research was supported by the Scientific and Technological Research Council of Turkiye (TÜBİTAK) under Grant No. 2219, awarded for the first author's postdoctoral research at the Tokyo Institute of Technology. The authors gratefully acknowledge the Disaster and Emergency Management Authority of Turkiye (AFAD) for providing the strong-motion data used in this study. Maps were generated using the Generic Mapping Tools (GMT). The 3D regional velocity model was developed, and all ground motion simulations and validation analyses were conducted by Dr. Bilal Özaslan under the supervision of Professor Hiroaki Yamanaka, utilizing a customized version of the FDM 3D code (Version 33) originally developed by Dr. Nobuyuki Yamada. The goodness-of-fit validation method applied in this work was based on the formulation proposed by John G. Anderson, with a modified implementation adapted by Dr. Seiji Tsuno to meet the specific objectives of this research. All simulations and data analyses were performed using the computational infrastructure and research facilities of the Tokyo Institute of Technology.

Author contributions Bilal Özaslan: Data processing, simulation, validation, visualization of data and results, writing the original draft. Hiroaki Yamanaka: Supervision, review and editing, technical guidance. Seiji Tsuno: Development and adaptation of validation tools, review and editing. Nobuyuki Yamada: Original FDM code development, technical support.

Funding Open access funding provided by the Scientific and Technological Research Council of Türkiye (TÜBİTAK). This work was funded by the Scientific and Technological Research Council of Turkiye (TÜBİTAK) under Grant No. 2219, supporting the first author's, B.O. postdoctoral research at the Tokyo Institute of Technology.

Data availability The strong-motion data utilized in this study were obtained from the Disaster and Emergency Management Authority of Turkiye (AFAD) and are publicly available through AFAD's data sharing platform upon request. The computational tools used in this research, including the customized FDM 3D simulation code (Version 33), are not publicly available but can be shared for academic purposes upon reasonable request to the corresponding author, subject to prior approval by the code developers and host institution.

Declarations

Conflict of interest The authors declare that there is no conflict of interest with respect to the research, authorship, or publication of this article.

References

Aki K, Larner K (1970) Surface motion of a layered medium having an irregular interface due to incident plane SH waves. J Geophys Res 75:933–954. https://doi.org/10.1029/JB075i005p00933

Anderson JG (2004) Quantitative measure of the goodness-of-fit of synthetic seismograms. In: Proc 13th World Conf Earthq Eng. Earthquake Engineering Research Institute, Vancouver, Paper 243

Bard PY, Bouchon M (1980) The seismic response of sediment-filled valleys. Part 1: the case of incident SH waves. Bull Seismol Soc Am 70(4):1263–1286

Bizzarri A (2014) On the point-source approximation of earthquake dynamics. Ann Geophys 57(3)

Bradley BA (2019) On-going challenges in physics-based ground motion prediction and insights from the 2010–2011 Canterbury and 2016 Kaikōura, new Zealand earthquakes. Soil Dyn Earthq Eng 124:354–364

Buckreis TE, Pretell R, Sandikkaya MA, Kale Ö, Askan A, Brandenberg SJ et al (2024a) Engineering attributes of ground motions from February 2023 Türkiye earthquake sequence. Earthq Spectra 40(4):2268–2284

Buckreis TE, Pretell R, Sandikkaya MA, Kale Ö, Askan A, Brandenberg SJ, Stewart JP (2024b) Engineering attributes of ground motions from February 2023 Türkiye earthquake sequence. Earthq Spectra 40(4):2268–2284

Campbell KW (2009) Estimates of shear-wave Q and κ0 for unconsolidated and semiconsolidated sediments in Eastern North America. Bull Seismol Soc Am 99(4):2365–2392

Chávez-García FJ, et al (2018) Site effects using methods based on lateral homogeneity and laterally heterogeneous media: an impossible marriage? Bull Earthq Eng (in press)

Disaster and Emergency Management Authority (AFAD) (2023) February 6, 2023 Pazarcık–Elbistan Kahramanmaraş earthquakes (Mw 7.7–Mw 7.6) report (in Turkish). https://deprem.afad.gov.tr/

Duman TY, Çan T, Emre Ö, Kadirioğlu FT, Başarır Baştürk N, Kılıç T et al (2018) Seismotectonic database of Turkey. Bull Earthq Eng 16:3277–3316

Graves RW (1996) Simulating seismic wave propagation in 3D elastic media using staggered-grid finite differences. Bull Seismol Soc Am 86(4):1091–1106

Graves RW (1998) Three-dimensional finite-difference modeling of the San Andreas fault: source parameterization and ground-motion levels. Bull Seismol Soc Am 88(4):881–897

Graves RA, Pitarka A (2015) Refinements to the graves and Pitarka (2010) broadband ground-motion simulation method. Seismol Res Lett 86(1):75–80. https://doi.org/10.1785/0220140101

Graves R, Pitarka A (2016) Kinematic ground motion simulations on rough faults including effects of 3D stochastic velocity perturbations. Bull Seismol Soc Am 106:2136–2153

Graves RW, Pitarka A, Somerville PG (1998) Ground-motion amplification in the Santa Monica area: effects of shallow basin-edge structure. Bull Seismol Soc Am 88(5):1224–1242

Graves R, Jordan TH, Callaghan S, Deelman E, Field E, Juve G, Milner K (2010) A physics-based seismic hazard model for Southern California. Pure Appl Geophys 167:367–381

Irikura K, Miyake H (2011) Recipe for predicting strong ground motion from crustal earthquake scenarios. Pure Appl Geophys 168:85–104. https://doi.org/10.1007/s00024-010-0150-9

Kawase H (1996) The cause of the damage belt in kobe: the basin-edge effect, constructive interference of the direct S wave with the basin-induced diffracted and Rayleigh waves. Seismol Res Lett 67(5):25–35

Khanbabazadeh H, Iyisan R (2013) A numerical study on the basin edge effect on soil amplification. Bull Earthq Eng 11:1305–1323

Khanbabazadeh H, Iyisan R, Özaslan B (2022) Seismic behavior of the shallow clayey basins subjected to obliquely incident wave. Geomech Eng 31(2):183–195. https://doi.org/10.12989/gae.2022.31.2.183

King JL, Tucker BE (1984) Observed variations of earthquake motion across a sediment-filled basin. Bull Seismol Soc Am 74(1):137–151

Maggi A, Priestley K (2005) Surface waveform tomography of the Turkish–Iranian plateau. Geophys J Int 160(3):1068–1080

Makra K, Chávez-García FJ (2016) Site effects in 3D basins using 1D and 2D models: an evaluation of the differences based on simulations of the seismic response of Euroseistest. Bull Earthq Eng 14(4):1177–1194

McCallen D, Petersson A, Rodgers A, Pitarka A, Miah M, Petrone F, Sjogreen B, Abrahamson N, Tang H (2021) EQSIM: A multidisciplinary framework for fault-to-structure earthquake simulations on exascale computers. Part I: computational models and workflow. Earthq Spectra 37(2):707–735

McCallen D, Pitarka A, Tang H, Pankajakshan R, Petersson NA, Miah M, Huang J (2024) Regional-scale fault-to-structure earthquake simulations with the EQSIM framework: workflow maturation and computational performance on GPU-accelerated exascale platforms. Earthq Spectra 40(3):1615–1652

Medved I, Polat G, Koulakov I (2021) Crustal structure of the Eastern Anatolia region (Turkey) based on seismic tomography. Geosciences 11(2):91

Mendoza C, Hartzell SH (1989) Slip distribution of the 19 September 1985 Michoacan, Mexico, earthquake: Near-source and teleseismic constraints. Bull Seismol Soc Am 79(3):655–669

Miyake H, Iwata T, Irikura K (2003) Source characterization for broadband ground-motion simulation: kinematic heterogeneous source model and strong motion generation area. Bull Seismol Soc Am 93:2531–2545

Moczo P, Kristek J, Bard PY et al (2018) Key structural parameters affecting earthquake ground motion in 2D and 3D sedimentary structures. Bull Earthq Eng 16:2421–2450

Ozaslan B, Iyisan R (2022) Determination of spectral aggravation factors in alluvial basins by nonlinear numerical analyses. J Fac Eng Archit Gazi Univ 37(1):247–263. https://doi.org/10.17341/gazimmfd.814370

Özaslan B, Haşal ME, Khanbabazadeh H, Akbaş M, İyisan R (2020) Dynamic response analysis of trapezoidal basins on numerical models. IOP Conf Ser Mater Sci Eng 960(4):042048. https://doi.org/10.1088/1757-899X/960/4/042048

Özaslan B, Iyisan R, Haşal ME, Khanbabazadeh H, Yamanaka H (2022) Assessment of the design spectrum with aggravation factors by 2D nonlinear numerical analyses: A case study in Gemlik Basin, Turkey. Bull Earthq Eng 20:1371–1395. https://doi.org/10.1007/s10518-021-01296-6

Ozer C, Ozyazicioglu M, Gok E, Polat O (2019) Imaging the crustal structure throughout the East Anatolian fault Zone, Turkey, by local earthquake tomography. Pure Appl Geophys 176:2235–2261

Özmen ÖT, Yamanaka H, Alkan MA, Çeken U, Öztürk T, Sezen A (2017) Microtremor array measurements for shallow S-wave profiles at strong-motion stations in Hatay and Kahramanmaraş Provinces, Southern Turkey. Bull Seismol Soc Am 107(1):445–455

Paolucci R, Smerzini C, Vanini M (2021) BB-SPEEDset: A validated dataset of broadband near-source earthquake ground motions from 3D physics-based numerical simulations. Bull Seismol Soc Am 111(5):2527–2545

Papageorgiou AS, Kim J (1991) Study of the propagation and amplification of seismic waves in Caracas Valley with reference to the 29 July 1967 earthquake: SH waves. Bull Seismol Soc Am 81(6):2214–2233

Petersson NA, Sjogreen B (2012) Stable and efficient modeling of an elastic Attenuation in seismic wave propagation. Commun Comput Phys 12:193–225

Petersson NA, Sjögreen B (2015) Wave propagation in anisotropic elastic media using summation-by-parts finite differences. J Comput Phys 299:820–841

Petrone F, Abrahamson N, McCallen D, Miah M (2021) Validation of (not-historical) large-event near-fault ground-motion simulations for use in civil engineering applications. Earthq Eng Struct Dyn 50(1):116–134

Pitarka A (1999) 3D elastic finite-difference modeling of seismic motion using staggered grids with nonuniform spacing. Bull Seismol Soc Am 89:54–68

Pitarka A, Graves R, Somerville P (2004) Validation of a 3D velocity model of the Puget sound region based on modeling ground motion from the 28 February 2001 Nisqually earthquake. Bull Seismol Soc Am 94(5):1670–1684

Pitarka A, Graves R, Irikura K, Miyakoshi K, Rodgers A (2020) Kinematic rupture modeling of ground motion from the M7 Kumamoto, Japan earthquake. Pure Appl Geophys 177:2199–2221

Pitarka A, Graves R, Irikura K, Miyakoshi K, Wu C, Kawase H, Rodgers A, McCallen D (2021) Refinements to the Graves–Pitarka kinematic rupture generator, including a dynamically consistent slip-rate function, applied to the 2019 Mw 7.1 Ridgecrest earthquake. Bull Seismol Soc Am 112(1):287–306

Semblat JF, Kham M, Parara E, Bard PY, Pitilakis K, Makra K, Raptakis D (2005) Seismic wave amplification: basin geometry versus soil layering. Soil Dyn Earthq Eng 25(7–10):529–538

Smerzini C, Amendola C, Paolucci R, Bazrafshan A (2023) Engineering validation of the BB-SPEEDset, a data set of near-source physics-based simulated accelerograms. Earthq Spectra 40(1):420–445

Smith WD (1975) The application of finite element analysis to body wave propagation problems. Geophys J Int 42:747–768

Somerville PG, Graves RW (2003) Characterization of earthquake strong ground motion. Pure Appl Geophys 160(10–11):1811–1828

Somerville P, Irikura K, Graves R et al (1999) Characterizing crustal earthquake slip models for the prediction of strong ground motion. Seismol Res Lett 70(1):59–80

Taborda R, Bielak J (2011) Large-scale earthquake simulation: computational seismology and complex engineering systems. Comput Sci Eng 13(4):14–27

Tezel T, Shibutani T, Kaypak B (2013) Crustal thickness of Turkey determined by receiver function. J Asian Earth Sci 75:36–45

Tsuno S, Nagashima F, Kawase H, Yamanaka H, Matsushima S (2023) Predicted results of weak and strong ground motions at the target site of the blind prediction exercise as steps-2 and −3. Earth Planet Space 75(1):130

Yamada N, Iwata T (2005) Long-period ground motion simulation in the Kinki area during the MJ 7.1 foreshock of the 2004 off the Kii Peninsula earthquakes. Earth Planet Space 57(3):197–202

Yamanaka H (1989) Study on seismic wave propagation in sedimentary layers with irregular interfaces. Dissertation, Tokyo Institute of Technology

Zeng Y, Anderson JO (1996) A composite source model of the 1994 Northridge earthquake using genetic algorithms. Bull Seismol Soc Am 86:S71–S89

Zhang B, Papageorgiou AS (1996) Simulation of the response of the Marina district Basin, San Francisco, California, to the 1989 Loma Prieta earthquake. Bull Seismol Soc Am 86(5):1382–1400

Zhang W, Zhang Z, Fu H, Li Z, Chen X (2019) Importance of Spatial resolution in ground motion simulations with 3-D basins: an example using the Tangshan earthquake. Geophys Res Lett 46(21):11915–11924

Zhu C, Thambiratnam D, Gallage C (2018) Statistical analysis of the additional amplification in deep basins relative to the 1D approach. Soil Dyn Earthq Eng 104:296–306

Zor E, Sandvol E, Gürbüz C, Türkelli N, Seber D, Barazangi M (2003) The crustal structure of the East Anatolian plateau (Turkey) from receiver functions. Geophys Res Lett 30:8044

Authors and Affiliations

Bilal Ozaslan[1] · Hiroaki Yamanaka[2] · Seiji Tsuno[2] · Nobuyuki Yamada[3]

✉ Bilal Ozaslan
bilal.ozaslan@ahievran.edu.tr

[1] Department of Civil Engineering, Kirsehir Ahi Evran University, Kirsehir, Türkiye

[2] Department of Architecture and Building Engineering, Tokyo Institute of Technology, Tokyo, Japan

[3] Research and Education Faculty Natural Science Cluster, Kochi University, Kochi, Japan